

Abstract

Accurate suspended sediment concentration measurements are key to understand and quantify the sediment transport patterns in the surf and swash zones. One of the most widely used instruments to collect suspended sediment concentrations is the Optical Backscatter Sensor (OBS). However, the OBS is known to give erroneous readings when deployed in bubbly environments like the surf zone. The present study aims to quantify the influence of an aerated wave breaking environment on the OBS sediment concentration measurements. Experiments are performed in a large wave flume, which ensures full air entrapment under plunging breaking waves, and avoids scale effects that could affect the volume of entrapped air, the air bubble penetration depth and the residence time of air bubbles in the post-breaking turbulent eddies. OBS measurements are obtained at 66 locations along a fixed bed profile for 14 regular breaking wave conditions. In the absence of suspended sediment particles, OBS voltage measurements are used as a proxy for air bubble content. The presented OBS results show peaks up to 1.49 V (31% of the OBS measurement range, corresponding to 16 g/l for sediment with $d_{50} = 0.25$ mm) produced by air bubbles in the most energetic tested wave breaking conditions, while the maximum time-averaged value obtained is 0.48 V (10% of the OBS measurement range, corresponding to 5 g/l). The results highlight the importance of considering the presence of air bubbles where OBS are deployed to measure suspended sediment concentrations. A good correlation is found between the breaker depth index and the air bubble distribution and two predictive formulas are derived to forecast the area of air bubble influence in the surf zone

1.- Introduction

The nearshore zone is characterized by strong currents and turbulent bubbly flows induced by wave breaking. The dynamics in this region are complex and their understanding is typically hampered by the lack of accurate and reliable measurements. Obtaining detailed measurements of water surface elevation, sediment concentration and sediment and water fluxes within the dynamic, highly turbulent and aerated wave breaking region is both a difficult and costly task [1, 2].

One of the most robust, reliable and frequently used equipment to recover suspended sediment concentrations in the surf and swash zones is the Optical Backscatter Sensor (OBS) [3]. An OBS is an optical sensor that measures turbidity and suspended sediment concentration by detecting the light backscattered from suspended matter. This sensor consist of a high intensity infra-red emitting diode, a detector, and a linear, solid state temperature transducer (D&A Manual, 1991 [4, https://s.campbellsci.com/documents/eu/technical-papers/obs_bubbles.pdf]). The OBS output signal

53 comes as a voltage which is converted to suspended sediment concentration (g/l) by means of a
54 calibration using sediment from the field site [5, 6]. However, light is scattered not only by sediment
55 particles, but also by air bubbles, as the refractive index of air is lower than the refractive index of
56 water. Consequently, high voltage readings by OBSs due to air bubble presence may falsely be
57 interpreted as suspended sediment events. Initial studies describing the performance of OBS sensors
58 [3, 7] reported a negligible influence of air bubbles on the sediment concentration signal. These initial
59 studies, involving bubbles produced by breaking ocean waves, were based on the assumption that the
60 largest air bubbles (those that produce highest backscatter) remain close to the water surface while
61 sediment transport processes occur near the bottom, which means that air bubbles do not significantly
62 affect sediment transport measurements. According to the OBS manual provided by the manufacturer
63 of the OBS-3+ used in the present study (D&A Instrument Company, acquired in 2007 by Campbell
64 Scientific), the effects of bubbles on OBS measurements is minimal [4]. However, several subsequent
65 studies have described non-negligible effects of air bubbles on OBS measurements [8, 9, 10]. Terrill
66 et al. (2001) [8] performed experiments designed to measure the effects of bubble size distribution on
67 the scattered light, and found that there is an increase in light backscatter as the void fraction induced
68 by wave breaking increases. Smith and Mocke (2002) [9] carried out a series of small-scale laboratory
69 measurements showing that air bubbles led to voltage readings that corresponded to sediment
70 concentration measurements up to 0.55 g/l, thus producing an erroneous average increase of 32 % in
71 the sediment concentration signal in their experiments. Puleo et al. (2006) [10] performed an
72 exhaustive experimental study including a variety of air bubble sizes (5 types), different water types
73 (fresh, synthetic and salty) and various kinds of sediment (mud and sand). The measurements, which
74 were conducted in a stirred tank generating air bubbles, showed a 25% increase in the OBS voltage
75 induced by air bubbles in the presence of sand and mud. This increase was even greater in synthetic
76 and salt water due to the longer residence times of air bubbles once the stirring in the tank was
77 stopped.

78 Air bubble entrainment during wave breaking in the ocean plays a role in several important
79 processes: it controls the transfer of heat and gas (including CO₂) at the air-sea interface; it influences
80 the transfer of turbulent energy during breaking; and it affects underwater acoustics. This is why the
81 presence of air bubbles or void fractions in the upper ocean layer has attracted recent research efforts
82 (i.e. Terrill et al. 2001 [8]; Kalvoda et al. 2003 [11]; Mori et al. 2007 [12]; Bell et al. 2017 [13] among
83 many others). In comparison to these open ocean studies, air bubble entrainment studies in the surf
84 zone are rather limited and usually done within laboratory small-scale conditions. Small-scale
85 experiments have some limitations in terms of accurately reproducing the prototype scale air bubble
86 entrainment owing to the difficulty of simultaneously satisfying the similitude requirements of

87 Reynolds number (the ratio between inertia and viscous forces), Froude number (the ratio between
88 inertia forces and gravity forces) and Weber number (the ratio between inertia and surface tension
89 forces). Most wave experiments are scaled to ensure similitude of Froude number between model and
90 prototype, as surface waves are gravity driven, but this limits the similitude of Reynolds and Weber
91 numbers between prototype and model. If fresh water is used and Froude similitude applied, the
92 viscosity and surface tension that control air bubble dynamics cannot be properly scaled. Chanson et
93 al. (2002) [14] showed that full-scale experiments are required to properly represent the air bubble
94 distribution under breaking conditions when fresh water is used as the experimental fluid. Moreover,
95 the above-mentioned similitude limitations also restrict scaling of the air entrainment volume (void
96 fraction) and momentum of air entrained bubbles within the fluid. The void fraction, size and
97 penetration depth of air bubbles depend on the jet velocity of the plunging breaker. Scaled
98 experiments underestimate the air entrainment velocity, reducing the amount, penetration depth and
99 size of the entrained bubbles. Similarly, the escape velocity of an air bubble from the fluid depends
100 largely on penetration depth and bubble size, which are both significantly affected by the scale of the
101 experiments.

102 The residence times of air bubbles depend mostly on their size. According to Monahan and Lu
103 (1990) [15] and Deane and Stokes (2002) [16], the life-time of bubbles can be divided into two stages:
104 the first stage where the air bubbles are introduced and fragmented by breaking waves, and the second
105 stage where the bubble plume evolves under the influence of turbulent diffusion, advection, buoyant
106 degassing and dissolution. Lamarre (1993) [17] and Lamarre and Melville (1992) [18] conducted
107 laboratory experiments to demonstrate that bubble plumes experience rapid transformation right after
108 breaking. Their measurements show that the volume of air enclosed in the initial air pocket is
109 preserved for up to 1/4 of the wave period after breaking, and that the plumes lose 95% of the initially
110 entrained air volume during the first wave period after breaking.

111 The aim of this paper is to investigate the effect of air bubbles on OBS measurements under large-
112 scale (prototype) breaking wave conditions. The focus is on plunging breaking waves, which will
113 produce a larger void fraction and bigger air bubbles than spilling waves [19]. The larger void
114 fractions at breaking will lead to the presence of a greater number of air bubbles at deeper water
115 depths, which are likely to interfere with OBS measurements in the surf zone. Under plunging
116 conditions, which are usually found in laboratory experiments studying barred beach profiles, air
117 bubble entrainment is mainly produced by: i) the interaction of the curling wave jet with the water
118 surface at the plunge point; ii) the air entrapped in the cavity of the collapsing plunging wave; and
119 iii) the splashes and turbulence entrainment produced by the secondary wave [16, 20 and 21]. A new
120 large-scale wave flume dataset is produced involving plunging breaking waves over a barred

121 topography. The experiments involved fresh filtered water and the beach profile consisted of a rigid
122 bottom in the absence of mobile sediments. Therefore, the OBS voltage measurements will depend
123 only on the backscatter caused by the air bubbles. The aim of this data set is to quantify the effect of
124 air bubbles on the OBS voltage signal under a variety of plunging wave breaking conditions, and to
125 provide recommendations for OBS deployment in breaking wave conditions. In order to reach this
126 objective, a predictive formula will be derived to determine the area where air bubbles may affect the
127 OBS readings.

128

129 **2.- Experimental Procedure**

130 **2.1 Experimental set-up and measuring equipment**

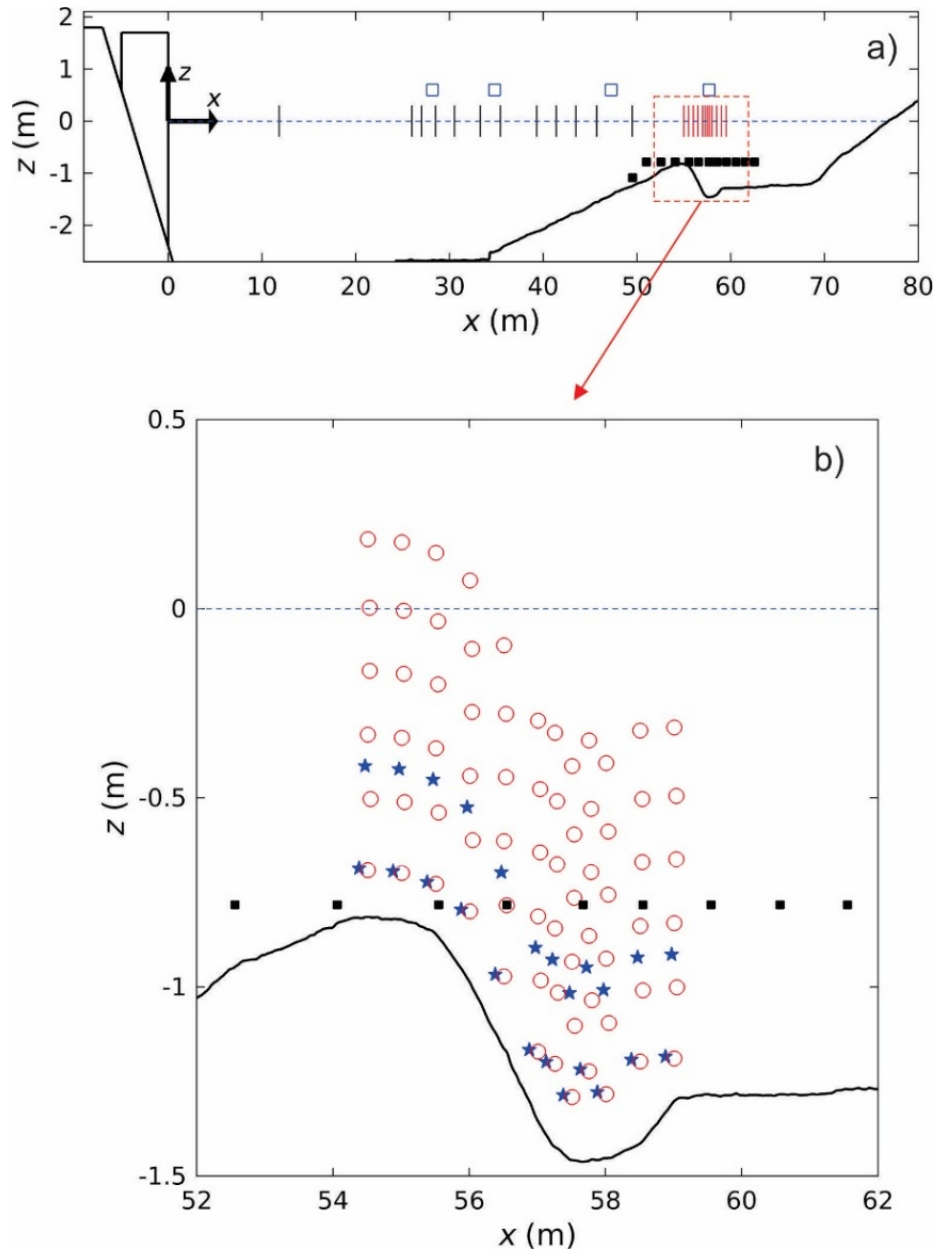
131 The experiments were performed in the CIEM wave flume at the Catalonia University of
132 Technology (UPC) in Barcelona, a 100 m long, 3 m wide and 4.5 m deep large-scale wave flume.
133 Figure 1 shows the rigid concrete bed profile, as well as the OBS and the water surface elevation
134 measurement positions. All test conditions had a still water level at the toe of the wave paddle of 2.65
135 m. The bottom profile started with a flat section of 35 m followed by a 1:12 offshore slope and a
136 breaker bar with a water depth at the bar crest of 0.81 m. The bar trough had a water depth of 1.46 m
137 (solid black line shown in Figure 1) and was followed by a 10 m long gentle slope (1:125) until the
138 profile reached a parabolic dissipative profile with an average slope of 1:7. The coordinate system
139 used in this study has its x -origin at the toe of the wave paddle and is defined positively towards the
140 beach; the vertical z -origin is at the still water level ($z=0$) and is defined positively upwards. The rigid
141 profile used here was the same profile as the one used in recent studies focusing on the hydrodynamics
142 under breaking waves [22, 23].

143 The water surface elevation was measured by means of Resistive Wave Gauges (RWG, solid blue
144 lines), Acoustic Wave Gauges (AWG, empty blue squares) and Pore Pressure Transducers (PPT, solid
145 black squares). The WGs and PPTs were deployed at fixed positions along the flume. The AWGs
146 were moved during the experimental campaign in order to increase the spatial resolution of the
147 measurements. For most of the wave conditions the water surface elevations were measured at 32
148 different locations in total. All water surface information data were directly acquired by the wave
149 paddle acquisition system at a sampling frequency of 40 Hz.

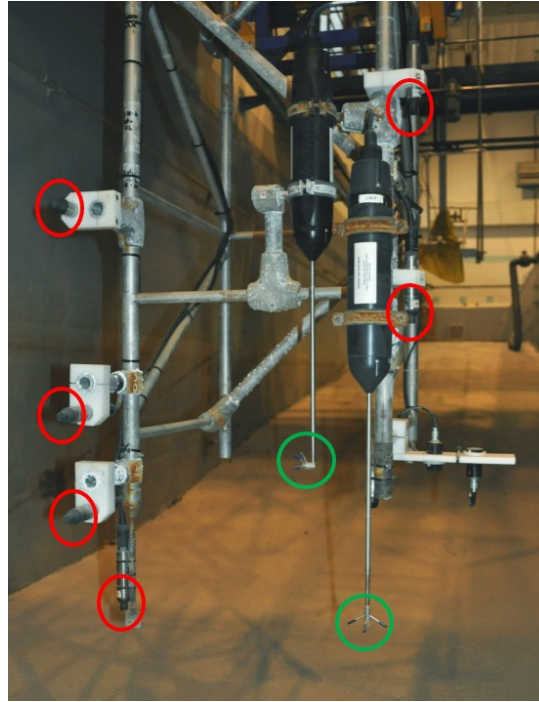
150 A mobile equipment carriage was used with a vertically moving frame from which several
151 instruments could be deployed (Figure 2). This mobile frame ensured positioning with +/- 1 cm
152 horizontal and +/- 1 mm vertical accuracy, and was instrumented with 2 ADVs (Nortek Vectrino), 6

153 OBSs and 1 PPT. The OBS on the frame had an equidistant spacing of 0.17 m in vertical direction,
154 while the ADVs had a distance between them of 0.27 m. The lowest OBS and ADV on the frame had
155 the same vertical positioning with a minimum distance to the bottom bed of 0.11 m. By repeating the
156 same wave condition while varying the position of the mobile frame a good spatial discretisation
157 along the wave breaking location (with a resolution of 0.5-0.25 m horizontally) has been obtained for
158 both velocity and OBS measurements. Figure 1 shows the locations of the mobile frame (red dashed
159 lines) during the experiments. The mobile frame was positioned at 12 different locations for the 3
160 conditions with the highest wave heights ($H=0.7$ and 0.8 m), and at 11 locations for all other tested
161 conditions. For each test condition, at least 66 different OBS observations within the breaking area
162 were collected.

163 The experimental procedure was as follows: 1) position the mobile frame at a pre-selected x -
164 location; 2) position the frame vertically at the required z distance from the bottom (corresponding to
165 the lowest OBS at 15 cm above the bed); 3) run the wave condition to be tested and check the acquired
166 data (if data was erroneous the run would be repeated); 4) move the frame vertically to a higher z
167 position (typically 8 to 9 cm higher) and repeat the same wave condition; 5) check the data before
168 moving the trolley with frame to the new x and z position.



170 Figure 1. Experimental configuration: a) Bed profile including the location of water surface elevation
 171 measurements: Wave Gauges (solid black lines), Pore Pressure Transducers (solid black squares) and Acoustic Wave
 172 Gauges (empty blue squares). Red lines show the x -location of the mobile frame (Acoustic Doppler Velocimeters and
 173 Optical Backscatter Sensors). b) Close-up of bar and trough section where the measurement grid of OBS (open red
 174 circles) and ADV (blue pentagrams) are presented. The solid black squares indicate the pressure transducers on the wall
 175 of the flume (as in subplot a).



178 Figure 2. Close-up of measurement frame which was attached to the mobile carriage. The red circles show the
 179 OBSs and ADVs are encircled in green.

180

181

182 2.2 Wave conditions

183 The waves were generated by a wedge-type wave paddle based on first-order wave generation.
 184 No absorption system was used for these experiments, as using it would have limited the stroke of
 185 the wave paddle for larger wave height/period combinations. The tested waves were regular and
 186 included different types of wave breaking, ranging from waves that travel over the bar with minor
 187 breaking and just a slight decrease of wave height along the bar, to the most energetic wave condition
 188 with $H=0.85$ m and $T=4$ s, which produced a strong plunging breaker and air bubbles that reached the
 189 bottom of the flume. The present paper will focus only on those wave conditions that resulted in wave
 190 breaking on the bar. Table 1 shows the wave height and period of the test conditions, as well as the
 191 surf similarity parameter $\xi_0 = \tan \beta / \sqrt{H_0/L_0}$, where $\tan \beta$ is the offshore bar slope (1/12), L_0 is the
 192 deep-water wave length and H_0 is the deep-water wave height [24]. All test conditions were visually
 193 classified as plunging breaking. This classification is consistent with the predictive classification
 194 proposed by Smith and Kraus (1991) [25] for wave breaking characteristics at barred beach profiles,
 195 corresponding to tests with 5° and 10° offshore bar slope angles.

196 Each experimental run had a duration of 10 minutes, which was enough to produce a quasi-steady

197 air bubble content produced by wave breaking at each location.

198

199

	H (m)	T (s)	ξ_0	H_0/L_0		H (m)	T (s)	ξ_0	H_0/L_0
M4_4	0.4	4	0.65	0.016	M5_6	0.5	6	1.02	0.007
M4_5	0.4	5	0.88	0.09	M6_3	0.6	3	0.39	0.047
M4_6	0.4	6	1.14	0.005	M6_4	0.6	4	0.53	0.024
M4_7	0.4	7	1.43	0.003	M6_5	0.6	5	0.72	0.013
M5_3	0.5	3	0.42	0.039	M7_3	0.7	3	0.36	0.055
M5_4	0.5	4	0.59	0.020	M7_4	0.7	4	0.49	0.028
M5_5	0.5	5	0.79	0.011	M85_4	0.85	4	0.45	0.034

200

Table 1. Information of tested wave conditions. Wave height (H); wave period (T); surf similarity parameter or Iribarren number (ξ_0); and offshore wave steepness (H_0/L_0).

201

202

203

2.3 Data processing

204

205

206

207

208

209

210

211

212

213

214

215

The water surface elevation was acquired by means of Resistive Wave Gauges, Acoustic Wave Gauges and Pore Pressure Transducers. The AWG data were despiked using a phase-space algorithm originally developed to despike ADV data in bubbly flows [26]. The Pore Pressure Transducers signal was converted to water surface elevation using linear wave theory (Tucker and Pitt 2001 [27] with the cut-off frequency obtained by Neumeier 2006 [28], 0.05-0.33 Hz). The ADV velocity data were despiked using the method developed by Goring and Nikora (2002) [29]. Low quality data, where signal-to-noise ratio and signal amplitude were below 15 and 75 dB respectively, were discarded. The ADV time series that produced a percentage of low quality data higher than 25% were discarded (the discarded data represented 16 time series out of 310 in total, i.e., 5%). Most of the discarded ADV time series had poor quality data due to the large number of air bubbles interfering with the ADV measurement positions, which occurred typically for the ADVs close to the water surface during the most energetic wave conditions.

216

217

218

219

220

For measurement locations around the crest of the bar, some OBS sensors were emerged during the trough phase of the waves. The OBS data reported in this paper are those that were completely submerged for more than 95% of the duration of the time series. In order to determine the submergence ratio of each OBS, its z -location was compared with the measured water surface elevation at each x OBS position.

221

In order to determine the threshold at which a peak will be considered as an air bubble event,

222 several benchmark experiments were performed to measure the OBS background noise. These
223 benchmark experiments included measurements in still water as well as measurements in the deeper
224 section of the flume under non-breaking waves and, hence, in the absence of air bubbles. Three OBSs
225 were used during these benchmark conditions and the noise level of the measurements, plus the
226 standard deviation of that noise, exhibited a mean voltage value of 0.0064 V. The upper measurement
227 limit of the OBS is at 4.8 V, and a value representing 2% of the upper limit was selected as a threshold
228 signal for the OBS equipment to detect air bubbles. This value, which corresponds to a voltage of
229 0.096 V, is 15 times higher than the computed background noise, and is therefore considered to be
230 high enough to assume that all OBS readings above this threshold will be produced by air bubbles.
231 This assumption was verified through benchmark tests involving 30-minute time series in still water
232 conditions and with non-breaking waves, in which no air bubble events (V above the 0.096 V
233 threshold) were detected.

234 The OBS data are reported in volts, and the measured events will be used as a proxy for air
235 bubbles. The light scatter measured by the OBS in the presence of air bubbles is controlled by the
236 number as well as the size of the air bubbles. Consequently, the OBS voltages cannot be correlated to
237 a physically meaningful variable such as void fraction or amount of bubbles. Similarly, it was decided
238 not to convert the OBS voltages to Suspended Sediment Concentrations, because the transformation
239 is dependent on the sediment characteristics and will therefore limit the applicability of the presented
240 values.

241 At the start of a run there is a transient phase which lasts less than 3 minutes, in which the wave
242 breaking location and wave breaking characteristics (including the water column air bubble content)
243 are not stable [30, 31]. Therefore, for each 10 min run the first 3 minutes of data were discarded, and
244 only the remaining 7 minutes of the time series were considered for further data analysis.

245

246 **3.- Water surface elevation and velocities under tested conditions**

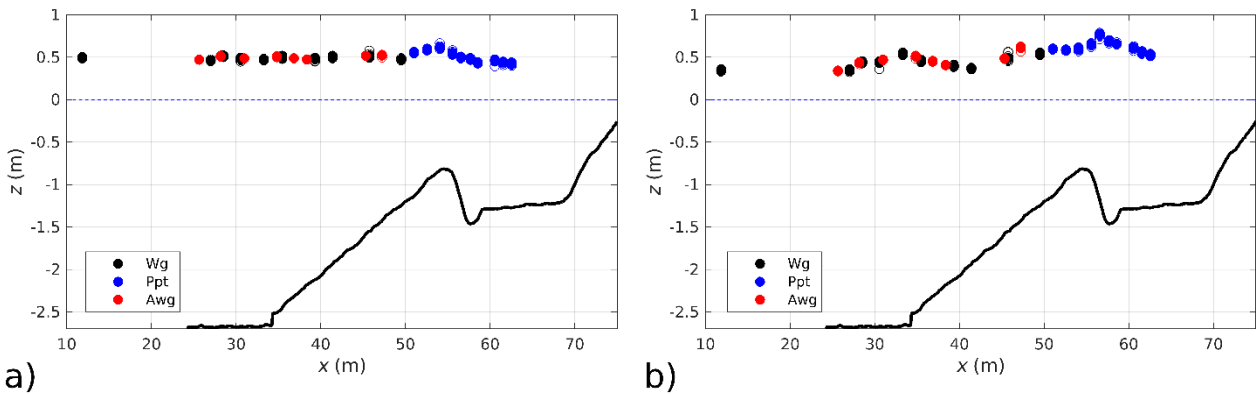
247 Before looking into the air bubble distribution measurements, it is important to describe first the
248 local hydrodynamics around the breaking location. Therefore, this section describes the wave
249 breaking process, the undertow and compares the results to previous wave flume experiments with a
250 barred profile.

251 All reported wave conditions produced wave breaking on top of the bar. Following a set of
252 preliminary tests, the measurement area was chosen to be between 54.9 and 60 m, which ranges from
253 the top of the bar crest up to 2 m shoreward of the bar trough. No wave absorption was activated

254 during these tests in order to use the full stroke of the wave paddle, thus allowing the paddle's largest
 255 wave height/period combinations. Wave height measurement repeatability was studied from the 11
 256 or 12 time series repeats of each condition (with the mobile frame at varying locations). The
 257 maximum standard deviation, considering all measurement positions and wave heights, was 0.05 m
 258 (for tests with $H=0.7$ and 0.85 m), while the mean standard deviation for each test condition,
 259 considering all the measurement points and repetitions performed, was 0.01 m. The excellent
 260 repeatability of the tested waves is shown in Figure 3, where the empty circles present the repeated
 261 tests measurements for the same wave conditions, and the solid circles represent the mean of the
 262 measured values.

263 Table 2 shows more detailed information about the wave breaking characteristics as well the
 264 location and magnitude of the maximum measured undertow velocity (v_{\max}), and the position at
 265 which this maximum undertow velocity was measured ($x_{v_{\max}}$). The most energetic tested condition
 266 throughout these tests, M85_4 corresponding to $H=0.85$ m and $T=4$ s, was the same wave condition
 267 as that previously described by van der A. et al (2017) [22] for the same bottom profile. A detailed
 268 analysis of the hydrodynamic processes is beyond the scope of the present paper. The reader is
 269 referred to van der A et al. (2017) [22] and van der Zanden et al. (2018) [23] for a more detailed
 270 description of wave heights, velocity fields, and turbulence distributions for the most energetic
 271 breaking wave condition.

272



273 Figure 3. Time-averaged wave heights for 11 test repeats (open circles) and mean wave height over all repeats
 274 (filled circle), for wave condition M5_3 (a), and M4_7 (b).

275

276

277

278

Tested waves	H_b (m)	Ω_b	γ_b	h_b (m)	x_{imp} (m)	v_{max} (m/s)	$x_{v\ max}$ (m)
M4_4	0.44	1.09	0.46	0.95		0.15	57.88
M4_5	0.59	1.69	0.62	0.95	57.4	0.25	58.88
M4_6	0.71	2.37	0.63	1.14	57.6	0.22	58.88
M4_7	0.60	2.31	0.42	1.43		0.22	57.88
M5_3	0.45	0.82	0.54	0.83	57.6	0.19	57.88
M5_4	0.56	1.11	0.59	0.95	57.4	0.28	57.88
M5_5	0.74	1.69	0.78	0.95	57.0	0.42	58.38
M5_6	0.83	2.22	0.73	1.14		0.40	58.88
M6_3	0.53	0.81	0.64	0.83	56.8	0.39	57.88
M6_4	0.69	1.14	0.73	0.95	56.5	0.39	57.88
M6_5	0.85	1.62	0.90	0.95	55.6	0.47	56.88
M7_3	0.65	0.85	0.78	0.83	56.5	0.47	58.38
M7_4	0.81	1.14	0.86	0.95	56.1	0.43	57.63
M85_4	0.99	1.15	1.05	0.95	54.9	0.63	56.47

279

280

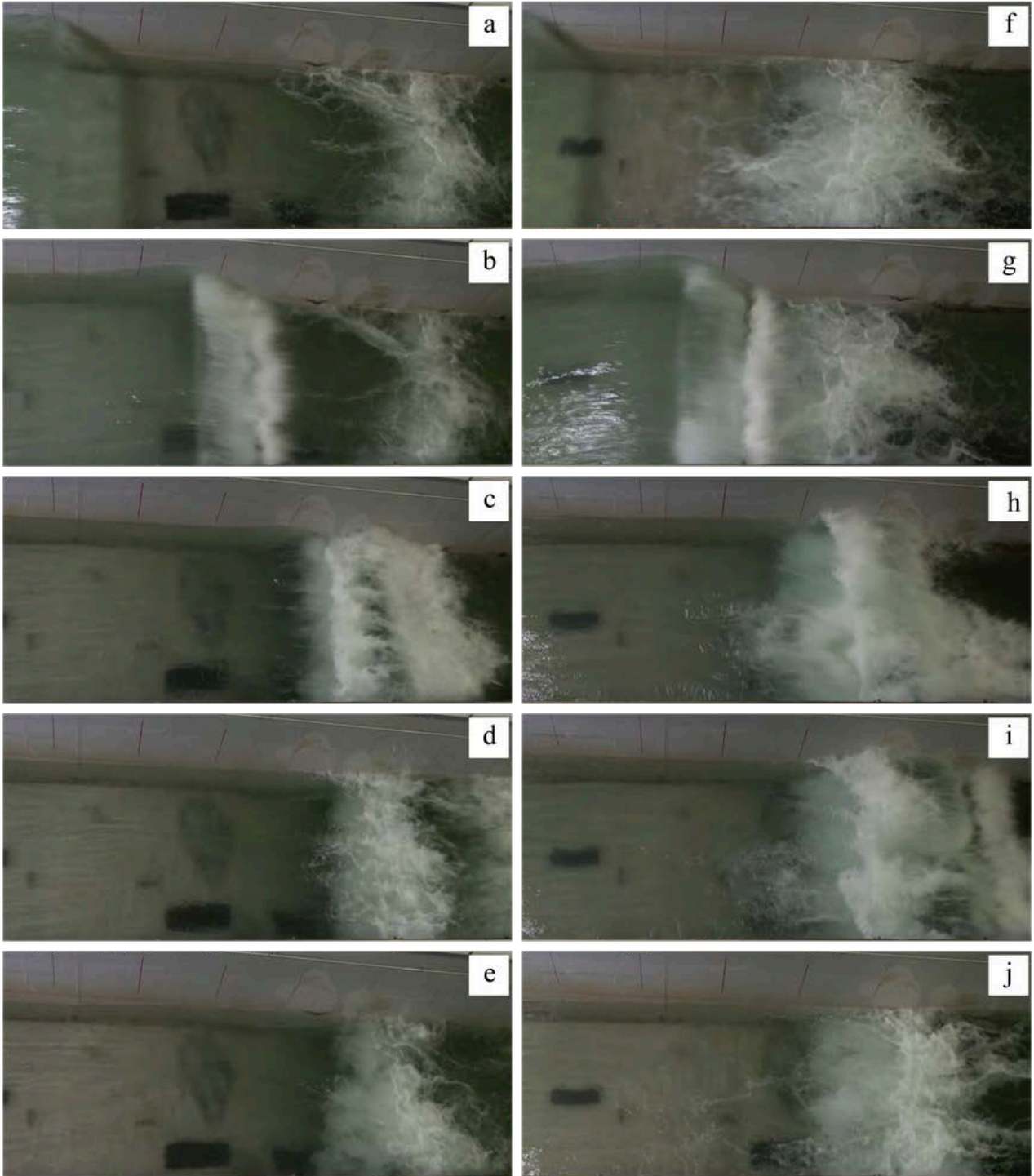
281

282

283

284

Table 2. Information on the tested wave conditions (targeted and measured across the study domain). Wave height at breaking (H_b); breaker height index (Ω_b , where $\Omega_b=H_b/H_0$); the absolute value of the water depth at breaking location (h_b); breaker depth index (γ_b computed as $\gamma_b=H_b/h_b$); impinging point location (x_{imp} , where the plunging jet hits the water surface); maximum measured undertow velocity (v_{max}) and position at which the maximum undertow was measured ($x_{v\ max}$).



286 Figure 4. Images of the wave breaking sequence acquired from video recordings (left M7_4 and right M85_4).

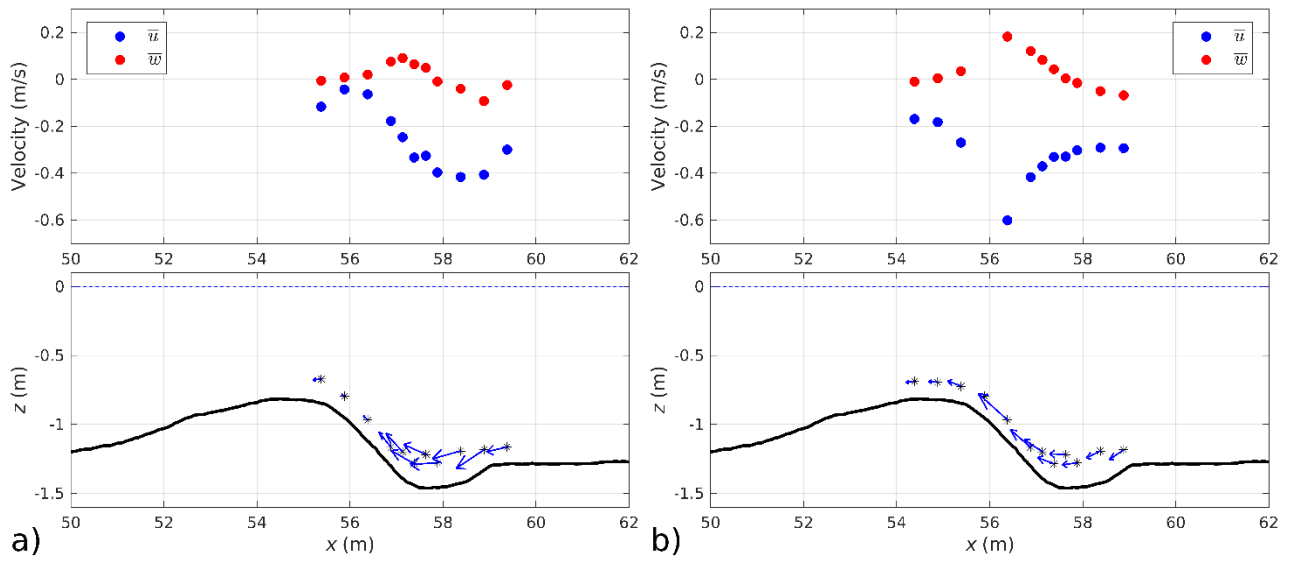
287

288 The wave breaking process for M7_4 and M85_4 is illustrated through a series of images in Figure
 289 4. The selected cases are among the most energetic tested waves, which produced high OBS voltage
 290 signals in the measurement area. The images correspond to different stages throughout the breaking
 291 process, starting at $t/T=0$ (4-a and 4-f) with the wave arrival on the left-hand side of each image. On

292 the right-hand side of both images (4-a and 4-f), one can still see traces of air bubbles from the
293 previous wave which are still trapped in the water column. The second frame of the sequence
294 corresponds to $t/T=0.15$ (4-b and 4-g), the moment at which the plunging jet hits the water surface
295 (the x -location of the impinging point is reported in Table 2). The next frames correspond to $t/T=0.33$
296 (4-c and 4-h) and show the final stage of the impinging jet penetrating the water column and creating
297 a secondary wave. This wave propagates shoreward and, in the subsequent frames ($t/T = 0.5$, 4-d and
298 4-i), it can be seen leaving the field of view on the right hand side. Finally, the last images (4-e and
299 4-j) correspond to $t/T=0.75$ and show air bubbles still remaining in the water column as they emerge
300 from the highly turbulent area.

301 The impinging positions in Table 2 were established using the video recording data. The images
302 were studied frame by frame using the reference points on the wall of the flume (which has a mark
303 for every meter) to determine the impinging positions. The blank spaces in Table 2 correspond to
304 conditions for which the impinging point could not be accurately established, since it occurred outside
305 the field of view of the fixed camera. Comparison of the impinging point and the location of the air
306 bubbles showed that the maximum air bubble peak always occurs onshore of the impinging point and
307 around the middle of the first splash roller (as previously also reported by Blenkinsopp and Chaplin
308 2007 [32] or Lim et al. 2015 [33]).

309 Undertow velocities were computed at all positions for each test, and the maximum undertow for
310 each wave condition is shown in Table 2 (v_{\max}). Maximum undertow velocities occur between the
311 trough of the bar and the bar crest, where the undertow negotiates the bar shape (Figure 5). The
312 undertow velocities match previous measurements performed by van der A et al. (2017) [22] for the
313 same profile and the same wave condition (M85_4). The differences between the van der A et al.
314 (2017) [22] experiments and those reported here reside in the shorter duration of the present time
315 series and the higher spatial and temporal distribution of velocity measurements performed by van
316 der A et al. (2017) [22].



318 Figure 5. Cross-shore (blue) and vertical (red) mean velocities are shown in the upper panel while the lower panel
 319 contains the bathymetric profile with the black solid line. The measurement position is indicated by a black star and the
 320 magnitude of the measurement by means of the blue velocity vector. The velocity measurements were performed at a
 321 mean distance of 15 cm from the bottom. a) for M5_5 ($H=0.5\text{m}$ and $T=5\text{s}$), and b) for M85_4 ($H=0.85\text{m}$ and $T=4\text{s}$).

322

323 4.- Air bubble content induced by wave breaking

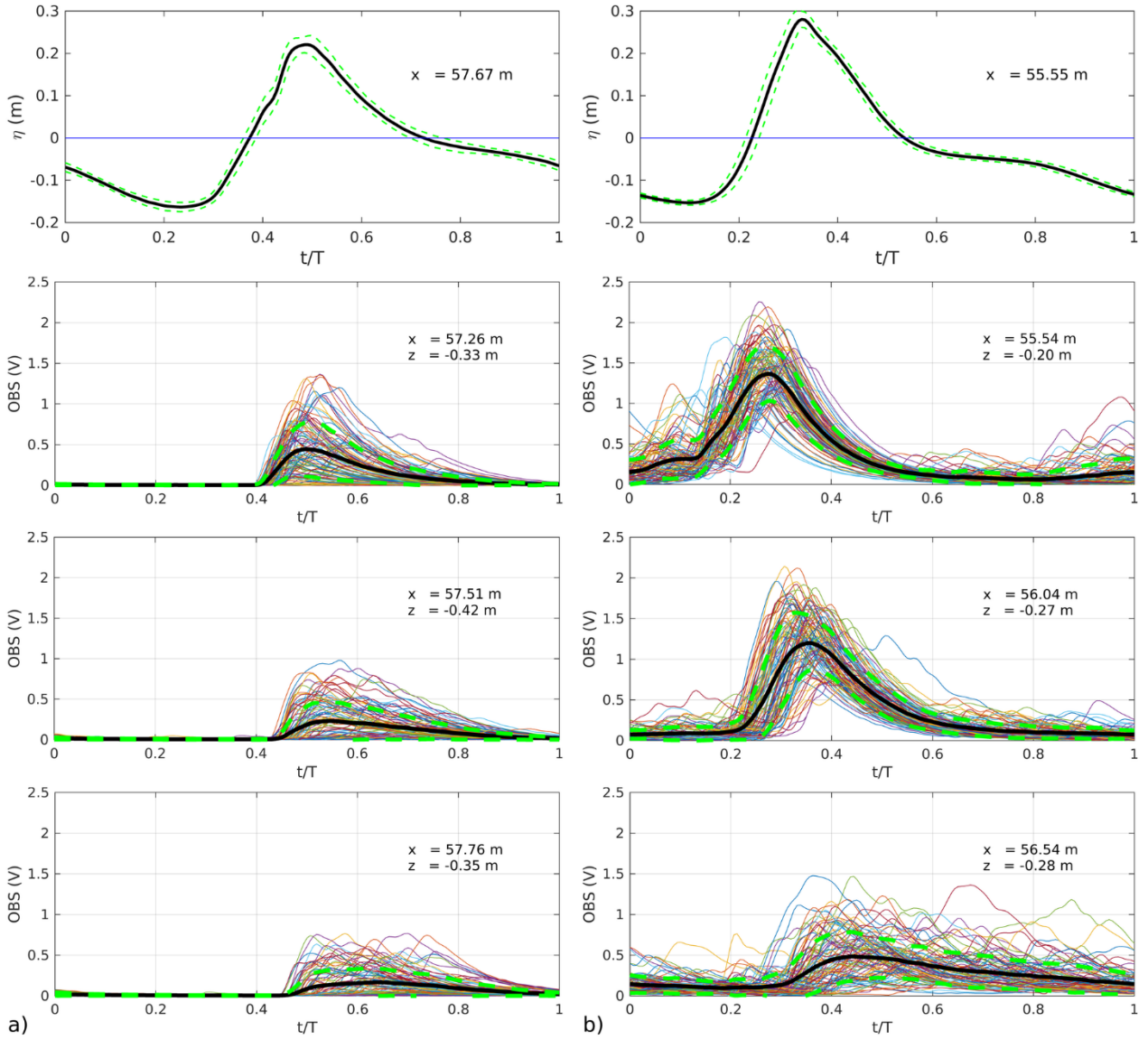
324 4.1 Air bubble measurements repeatability

325 Previous experiments illustrated the good repeatability of wave height and velocity measurements
 326 within the CIEM flume over mobile bed [34, 35] and fixed bed conditions [23]. In order to study the
 327 air bubble content repeatability, the present paper will study wave-by-wave OBS voltage repeatability
 328 for a monochromatic wave time series, as well as the repeatability of the OBS mean voltage for
 329 different runs of the same wave time series. Note that the OBSs measure the backscatter caused by
 330 air bubbles moving upwards due to buoyancy, but with a strongly 3D movement induced by the highly
 331 turbulent flow due to wave breaking [21]. Therefore, it is expected that OBS measurements present
 332 lower repeatability than water surface elevation and velocity measurements.

333 The wave-by-wave repeatability of air bubble measurements along a time series was evaluated
 334 considering the phase-average ensemble of each OBS time series. The zero-up crossing of the water
 335 surface at the most offshore pressure sensor was used to compute the phase-average times at each
 336 OBS. The OBS ensembles were time-referenced with these zero-up crossing points, in such a manner
 337 that $t/T=0$ corresponds to the zero-up crossing of the water surface. Figure 6 shows the ensemble-
 338 averaged of water surface elevation on the upper row, and the OBS signals on the following rows at

339 three different x -locations for two different wave conditions (M6_4 and M85_4, both with a 4 s
340 period). Results are presented here for the uppermost OBS, i.e. the one closest to the water surface,
341 which is the sensor most exposed to bubbles. At this elevation, the number of events within the time
342 series that measure air bubble peaks over the fixed threshold is significant (between 68-94% and
343 100% of waves produce voltage peaks over the threshold for M6_4 and M85_4 respectively). In
344 addition, due to the larger turbulence close to the water surface, the air bubble events are strongly
345 mixed, thus increasing the standard deviation (dashed cyan lines) of the events relative to the
346 computed mean (black thick line) of the ensemble. There is a correlation between the air bubble
347 distribution along the water column and the wave breaking induced turbulence, as previously shown
348 by Mori et al. (2007) [12] or Lim et al. (2015) [33]. Another source of turbulence will come from the
349 air bubbles entering and passing through the water volume, which inject and transfer energy into the
350 flow, increasing the turbulent kinetic energy (TKE) production [33]. After comparing the air bubbles
351 distribution with the TKE values computed by van der A. et al. (2017) [22] for M85_4, there is a
352 correlation between larger TKE values and larger dispersion of peak events across the mean ensemble
353 average (and with longer residence times of air bubbles within the water column).

354



355 Figure 6. Phase-averaged water surface elevation (upper row) and OBS output (following rows) for different wave
 356 conditions: a) for $H=0.6$ m and $T=4$ s (M6_4), OBS at $x=57.26$, 57.51 and 57.76 m from top to bottom; b) for $H=0.85$ m
 357 and $T=4$ s (M85_4), OBS at $x=55.54$, 56.04 and 56.54 m from top to bottom. The black thick line shows the mean of the
 358 ensembles, while the dashed green lines indicate the standard deviation.

359
 360 Table 3 quantifies the information presented in Figure 6, with P_{peaks} being the percentage of waves
 361 that produce air bubble events (an air bubble peak or event occurs when the OBS voltage exceeds the
 362 threshold of 0.096 V, i.e., $P_{\text{peaks}} = 94\%$ means that 94% of the arriving waves produce a voltage peak
 363 higher than 0.096 V). $\langle Oo_p \rangle$ is the mean of the OBS voltage of all peaks (where the angle brackets
 364 represent averaging over the entire time series). Std_p is the standard deviation of the measured peaks.
 365 Table 3 shows the OBS locations where the maximum voltages are measured as well as the next two
 366 shoreward OBS locations. The position with the highest voltage measurement correlates with the
 367 position with maximum P_{peaks} ($x=57.26$ m for M6_4 with $P_{\text{peaks}}=94\%$, and $x=55.54$ m for M85_4 with

368 $P_{peaks}=100\%$) and is always located after the impinging point of the breaking wave (cf. Table 2). In
 369 the M6_4 tested waves, there is a decrease in P_{peaks} while moving shoreward from the breaking
 370 position. Similarly, there is a decrease in $\langle Oo_p \rangle$ and Std_p . M85_4 presents a more energetic breaking
 371 condition, where a larger amount of air is entrained throughout the wave breaking process, thereby
 372 increasing the area in which air bubbles can be found and the duration of the air bubble events. All
 373 measured waves produce air bubble peaks at the three locations presented for M85_4, and the
 374 standard deviation relative to the computed mean values ($\langle Oo_p \rangle$) is lower than for M6_4. While it
 375 was close to 79% for M6_4, it is now 28% ($Std_p/\langle Oo_p \rangle$), on average over all studied locations).
 376 Despite significant differences in the air entrainment ratio induced by both wave breaking conditions
 377 (M6_4 and M85_4), there is a high repeatability of air bubble events after the breaking point with
 378 constant air entrainment at the same locations, low Std_p and constant repetition of the air bubble peaks
 379 within the wave phase.

380

	x (m)	P_{peaks} (%)	$\langle Oo_p \rangle$ (V)	Std_p (V)
M6_4 ($H=0.6$ m, $T=4$ s)	57.25	94	0.53	0.34
	57.50	68	0.30	0.25
	57.75	68	0.25	0.22
M85_4 ($H=0.85$ m, $T=4$ s)	55.50	100	1.49	0.30
	56.00	100	1.41	0.32
	56.50	100	0.68	0.28

381 Table 3. Computed air bubble OBS values. P_{peaks} indicates the percentage of waves that produce air bubble events
 382 (an air bubble event occurs when the OBS voltage goes beyond the threshold of 0.096 V), the mean of the measured
 383 peaks $\langle Oo_p \rangle$ and, lastly, the standard deviation of the measured peaks (Std_p).

384

385 The repeatability of air bubble events is now studied by repeating the times series of one wave
 386 condition. Table 4 presents the statistics of three considered parameters: time average OBS output in
 387 voltage $\langle Oo \rangle$, the percentage of waves that produce air bubble events P_{peaks} , and lastly the mean of
 388 the measured peaks over a time series $\langle Oo_p \rangle$. Due to time constraints, only one wave condition was
 389 repeated while the trolley was located around the area where most air bubbles could be seen. The
 390 percentage of differences (Eq. 1) is used to evaluate the repeatability of the acquired data. When
 391 considering the percentage difference for the time averaged OBS voltage ($\langle Oo \rangle$) for M85_4, the
 392 maximum difference between the various OBSs (each OBS presenting information for a different z
 393 location) is 23%, while the mean difference is 14%. The percentage difference for P_{peaks} has a
 394 maximum value of 20% and a mean value of 8%. Finally, the percentage difference for the mean

395 concentration of peaks ($\langle Oo_p \rangle$) has a maximum value of 14% and a mean value of 6%.

396

397 Eq. 1 $\frac{|V_1 - V_2|}{\frac{(V_1 + V_2)}{2}} \times 100 = \text{Percentage difference}$

398

Test numbers and conditions	Obs	$\langle Oo \rangle$ (V)	P_{peaks} (%)	$\langle Oo_p \rangle$ (V)
M85_4 ($H=0.85$ m, $T=4$ s)	1 (-0.69 m)	0.016 // 0.015	26 // 23	0.08 // 0.08
	2 (-0.50 m)	0.048 // 0.060	58 // 71	0.26 // 0.30
	3 (-0.33 m)	0.146 // 0.150	99 // 99	0.78 // 0.77
	4 (-0.16 m)	0.464 // 0.369	100 // 100	1.60 // 1.49

399 Table 4. OBS voltage signal (as a proxy for air bubbles) acquired at $x=55.5$ m. Only the lower 4 OBSs are shown,
 400 i.e. those presenting a submergence ratio higher than 95% of the computed time. Red values for the first time the time
 401 series was run and black values for repetition. The grey value in brackets next to the OBS number denotes the
 402 submergence distance to still water level in m.

403

404 When comparing the obtained results of Table 4 and 3 it is evident that the variability of OBS
 405 measurements between repeats of the same test (Table 4) is lower than the variability of the measured
 406 parameters within the time series of one test repeat (Table 3). This implies that the statistics obtained
 407 over one test repeat are sufficiently converged.

408

409 **4.2 Horizontal and vertical variability of air bubbles effects**

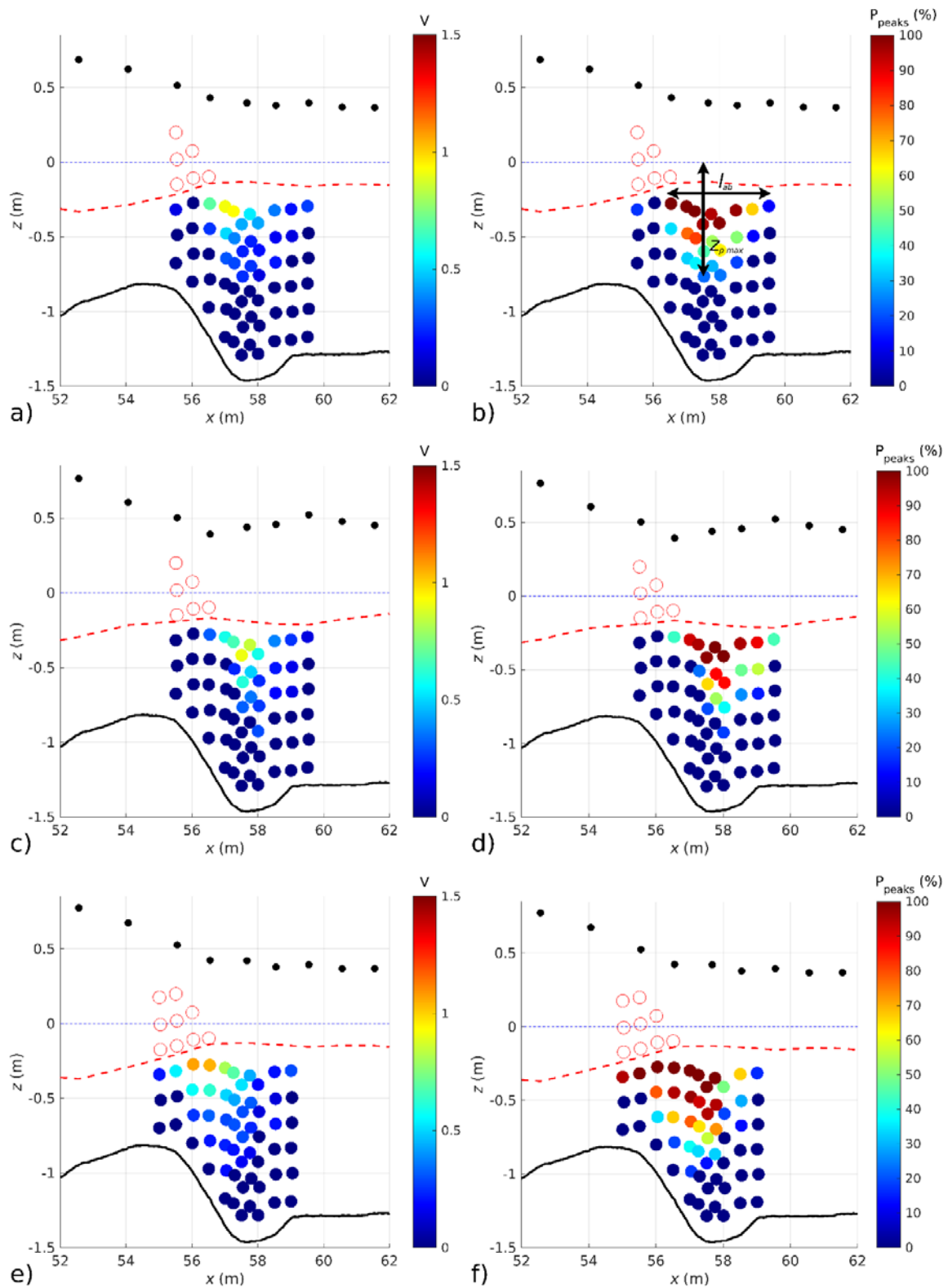
410 After presenting the repeatability of the OBS for capturing air bubble events, Figures 7 and 8
 411 show the spatial variation of the air bubble events for those test conditions that produced a larger
 412 distribution of OBS air bubble peaks ($P_{\text{obs}} > 30\%$, where P_{obs} is the variable that denotes the percentage
 413 of OBSs that measure air bubble peaks). Figures 7 and 8 show a different wave condition for each
 414 row: the plots on the left show the mean of the V computed during the peaks measured at each
 415 location; and the plots on the right show the P_{peaks} to present the distribution of air bubble events
 416 across the study area. The red dashed line shows the minimum envelope of the wave troughs and the
 417 black dots show the wave height. The OBSs that have not been coloured (empty red circles) are those
 418 that were emerged for $>5\%$ of the time, and were therefore excluded from the present analysis.

419 Table 5 shows the summary of data collected from all test conditions. Note that the data of OBSs
 420 that were emerged more than 5% of the measurement time were discarded (empty red circles in

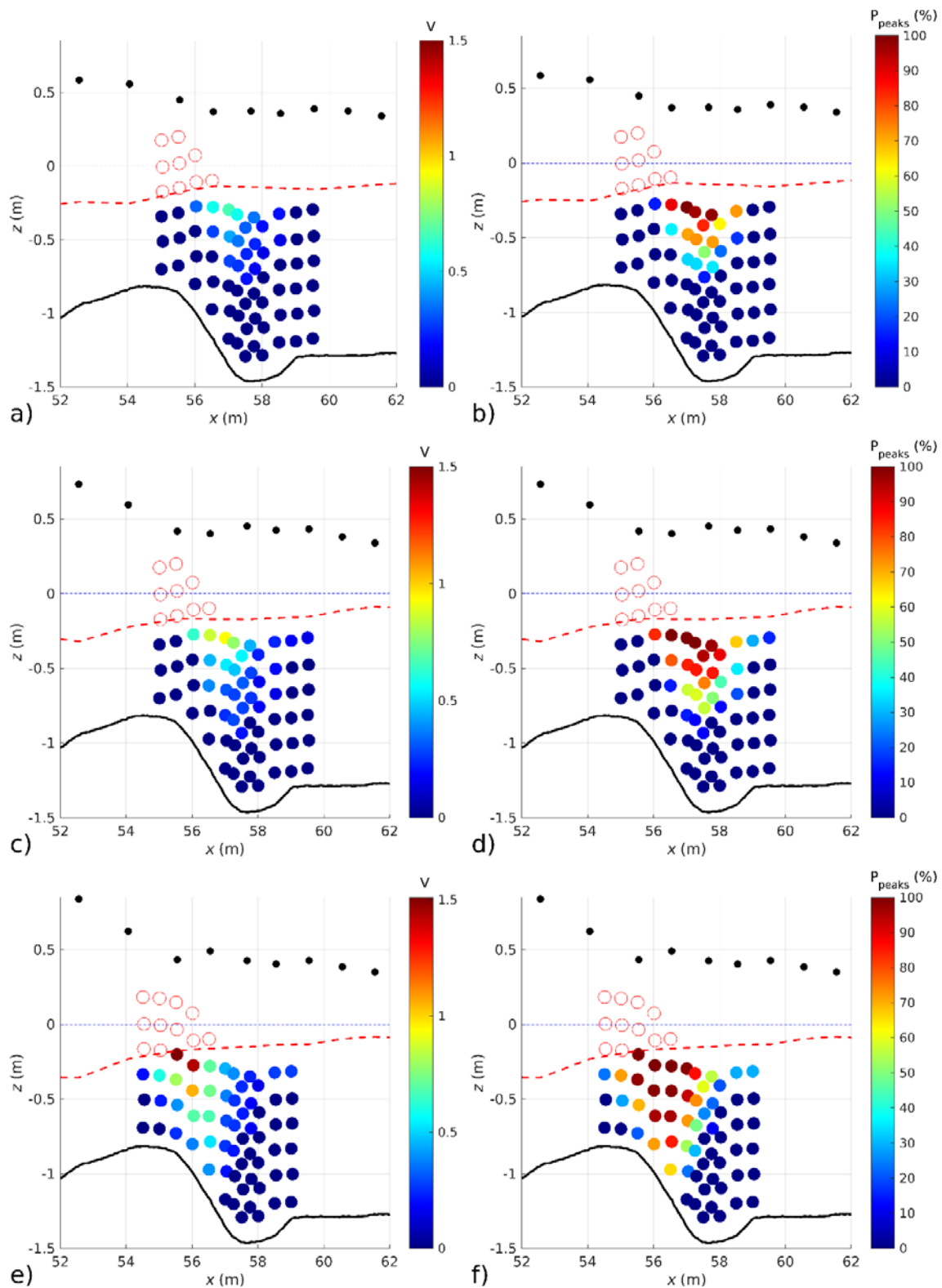
421 Figures 7 and 8), as well as the OBSs that showed voltage peaks for less than 10% of the waves (a
422 low percentage of air bubble events was discarded in order to avoid outliers distorting the mean
423 values). Table 5 shows two different types of variables: the first ones are local variables (white
424 background) that show information averaged in time at a unique location within the grid of OBS
425 measurements for each test condition, while the second ones are global variables (grey background)
426 that present a double average (in time and space) in order to provide information of the complete
427 study area. The local variables include: the maximum peak voltage measured along the measurement
428 grid ($\langle Oo_p \rangle_{max}$); the penetration depth, $z_{p\ max}$, indicating the absolute value of the maximum depth
429 where the OBSs were able to measure air bubble peaks (OBS signal $> 0.096\ V$) for more than 10%
430 of waves; and the dimensionless variable obtained from the ratio between $z_{p\ max}$ and H . The global
431 variables include the percentage of OBSs that measure peaks (P_{obs}), and the temporally and spatially
432 averaged OBS voltage $\overline{\langle Oo_p \rangle}$ where the overbar represents a spatial average. Therefore, the latter
433 indicates the mean of the air bubbles peaks measured by the OBS in the study area.

434

435



436 Figure 7. Optical backscatter measurements for M5_5, M5_6 and M6_5 waves from top to bottom respectively. The
 437 left-hand side panels (a, c and e) show the maximum voltage measured at each location. The right-hand side panels (b,
 438 d, e) show the percentage of waves producing a peak in OBS signal at each location. The solid black line shows the
 439 concrete bottom. The blue dashed line shows the still water level, the red dashed line the minimum of the wave troughs
 440 and the black dots the wave height.



441 Figure 8. Optical backscatter measurements for M7_3, M7_4 and M85_4 waves from top to bottom respectively. The
 442 left-hand side panels (a, c and e) show the maximum voltage measured at each location. The right-hand side panels (b,
 443 d, e) show the percentage of waves producing a peak in OBS signal each location. The solid black line shows the
 444 concrete bottom. The blue dashed line shows the still water level, the red dashed line the minimum of the wave troughs
 445 and the black dots the wave height.

Tested waves	H_b (m)	$\langle Oo_p \rangle_{\max}$ (V)	$z_{p \max}$ (m)	$z_{p \max}/H$	P_{obs}	$\overline{\langle Oo_p \rangle}$ (V)
M4_4 ($H=0.4$ m, $T=4$ s)	0.44	0.13	0.15	0.38	2 %	
M4_5 ($H=0.4$ m, $T=5$ s)	0.59	0.44	0.60	1.50	13 %	0.29
M4_6 ($H=0.4$ m, $T=6$ s)	0.71	0.32	0.41	1.03	8 %	
M4_6 ($H=0.4$ m, $T=7$ s)	0.60	0.21	0.41	1.03	8 %	
M5_3 ($H=0.5$ m, $T=3$ s)	0.45	0.15	0.41	0.82	2 %	
M5_4 ($H=0.5$ m, $T=4$ s)	0.56	0.21	0.42	0.84	7 %	
M5_5 ($H=0.5$ m, $T=5$ s)	0.74	0.93	0.76	1.52	40 %	0.35
M5_6 ($H=0.5$ m, $T=6$ s)	0.83	0.91	0.92	1.84	35 %	0.39
M6_3 ($H=0.6$ m, $T=3$ s)	0.53	0.32	0.59	0.98	12 %	0.22
M6_4 ($H=0.6$ m, $T=4$ s)	0.69	0.53	0.70	1.17	28 %	0.29
M6_5 ($H=0.6$ m, $T=5$ s)	0.85	1.07	0.98	1.63	56 %	0.38
M7_3 ($H=0.7$ m, $T=3$ s)	0.65	0.66	0.76	1.09	31 %	0.32
M7_4 ($H=0.7$ m, $T=4$ s)	0.81	0.94	0.93	1.33	45 %	0.38
M85_4 ($H=0.85$ m, $T=4$ s)	0.99	1.49	0.98	1.15	55 %	0.48

447 Table 5. Measured wave height and air bubble content information for all tested conditions: Wave height at
 448 breaking (H_b); maximum of the $\langle Oo_p \rangle$ values computed along the measurement grid ($\langle Oo_p \rangle_{\max}$); the maximum
 449 penetration depth ($z_{p \max}$) is computed as the absolute value of the maximum depth where the OBSs measure air bubbles
 450 for more than 10% of the waves; relative penetration depth as ratio of $z_{p \max}$ and H ; percentage of OBSs that present
 451 peaks over the 0.096 V threshold (P_{obs}); and the mean value of the voltage peaks over all OBS locations ($\overline{\langle Oo_p \rangle}$).

452

453 P_{obs} also provides information of the distribution of air bubbles across the study area. All tests in
 454 Table 5 report air bubble events around the impinging point. Even the two cases that present a lower
 455 number of OBSs measuring air bubble events, $P_{\text{obs}}=2\%$, which represent a single OBS measuring air
 456 bubble events, have values of 0.13 and 0.15 V as mean of the computed peaks for that OBS voltage.
 457 These measurements represent values around 1.4 g/l when converted to Suspended Sediment
 458 Concentrations (OBSs calibrated with $d_{50}=0.25$ mm sediment from the CIEM wave flume). Even if
 459 the peaks are local and do not appear constantly in the time signal, their values would be significantly
 460 high to distort Suspended Sediment Flux computations over the water column. For six out of the 14
 461 tests in Table 5 the air bubble events occurred at more than 30% of the OBS measurement locations
 462 ($P_{\text{obs}}>30\%$). These tests, where air bubble events are more spread out across the study area, exhibit
 463 larger V values (as a proxy for air bubbles) and a larger percentage of waves producing air bubble
 464 events. These tests provide the most reliable data for the study of penetration depth and bubble length
 465 distribution, for comparison with previous data sets.

466 An important parameter to assess the air bubble impact in OBS locations is the penetration depth

467 of air bubbles. Table 5 shows the penetration depth, $z_{p \max}$, defined as the absolute value of the
468 maximum depth where the OBSs measure air bubbles for more than 10% of the waves (plotted in
469 Figure 7-b). The air bubbles were seen to reach the bottom of the flume in the trough area ($x=58$ m)
470 for the most energetic tested condition ($H=0.85$ m and $T=4$ s), so it is expected that the air bubbles
471 would have reached larger $z_{p \max}$ if the bar trough had been deeper. The average penetration depth
472 over all tests was $1.16H_0$ (with a standard deviation value of $0.38H_0$). The maximum penetration
473 depth was $1.84H_0$ for test condition M5_6, while the minimum penetration depth was $0.38H_0$ for
474 condition M4_4. When considering only those wave conditions that show OBS peaks for more than
475 30% of the measuring points, the mean penetration depth increases up to $1.43H_0$ (with a standard
476 deviation value of $0.29H_0$). These measured values are in range with previous small scale experiments
477 that exhibit penetration depths from $0.5H_0$ [36, 33] to values of up to $2.4H_0$ in Blenkinsopp and
478 Chaplin (2007) [32].

479 The bubble cloud length, l_{ab} , indicates the longitudinal distance over which OBSs measure air
480 bubble peaks for more than 10% of the arriving waves (as presented in Figure 7-b). Table 6 reports
481 the length of air bubble clouds and the bubble area entrapped along the breaking area. The data
482 presented show the characteristics of the larger events ($P_{obs}>30\%$) as these are cases that produce
483 larger air bubble events and are therefore more easily captured by OBSs. The air bubble area (A_{ab}) is
484 defined as the area where the air bubbles are measured between the maximum penetration depth and
485 the wave trough. The lengths and area of the air bubbles shown in the table could have been larger
486 for some cases if the measurement grid had been extended. The columns x_{init} and x_{end} report the
487 information relating to the beginning and end of the air bubble plume. The information in brackets
488 after x_{init} and x_{end} shows that P_{peaks} values at these positions were greater than 10% (in brackets the
489 P_{peaks} values). The collected bubble distribution length l_{ab} has an average value of $0.12L_0$. This value
490 is in the same region as previous small-scale laboratory observations. For instance, Lim et al. (2015)
491 [33], reported a bubble cloud length between $0.1L_0$ and $0.7L_0$. According to Kalvoda et al. (2003)
492 [11], the maximum cloud lengths at the top and side view are $0.1L_0$ and $0.16L_0$ respectively.

493

Tested waves	l_{ab} (m)	x_{init}	x_{end}	A_{ab} (m^2)	max t/T
M5_5 ($H=0.5$ m, $T=5$ s)	2.97	56.54	59.51 (12%)	3.41	0.37
M5_6 ($H=0.5$ m, $T=6$ s)	2.97	56.54	59.51 (44%)	3.01	0.30
M6_5 ($H=0.6$ m, $T=5$ s)	4	55.01 (94%)	59.01 (16%)	3.58	0.57
M7_3 ($H=0.7$ m, $T=3$ s)	2.47	56.04	58.51	2.56	0.52
M7_4 ($H=0.7$ m, $T=4$ s)	3.47	56.04	59.51 (16%)	3.51	0.47
M85_4 ($H=0.85$ m, $T=4$ s)	4.5	54.51 (24%)	59.01 (29%)	3.88	1

495 Table 6. Main parameters of air bubble plumes. Length of the air bubble plumes measured in the upper layer of
496 OBS and bubble area computed considering the bubble penetration depth and the wave trough. Max t/T indicates the
497 maximum duration of the OBS ensemble average signal measuring over the V threshold, reporting the maximum
498 duration of the air bubble events over the OBS grid.

499

500 Previous laboratory experiments described by Kalvoda et al. (2003) [11] presented maximum air
501 bubble duration between $0.25T$ and $0.5T$. Similarly, Lamarre (1993) [17] reported experimental data
502 where the bubble duration expands up to $0.5T$ and where the plume is very compact with high void-
503 fraction concentrations and a subsequent void-fraction decrease. Table 6 shows the maximum
504 duration of air bubbles presence t/T measured during the present experiments. These data have been
505 computed by considering the time that the OBS mean ensemble signal exceeds the settled voltage
506 threshold. Within the presented large-scale data, which includes plunging breaking waves with wave
507 heights significantly larger than previously presented small-scale data sets and, therefore, larger
508 penetrations depths, the concentration of air bubbles within the time phase will largely depend on the
509 depth of the measurement probe and its position from the impinging point. For OBS locations closer
510 to the water surface, comparable to previous experimental data, and close to the impinging point, the
511 air bubbles produce OBS measurements beyond the settled threshold with maximum spans that go
512 up to $0.57T$. The exception to this behaviour is obtained for the most energetic tested case (M85_4),
513 where OBSs retrieve voltage signals over $0.75T$ at several positions and at one position, the signal
514 exceeds the threshold during the entire wave period. For the latter case, the ensemble-averaged OBS
515 signal can be seen in the lower panel of Figure 6-b. While this signal does not produce the largest
516 peaks in OBS measurements, it exhibits the longest air bubble residence times. Note that this location,
517 above bar trough, is also characterized by maximum TKE values [22], which may contribute to
518 vertical mixing of air bubbles and contribute to the high bubble residence times. These values are also
519 corroborated by the images presented in Figure 4. Panel f in Figure 4 ($t/T=0$) shows the new wave
520 arriving on the left-hand side of the image, and the residual bubbly area at the right of the image
521 (trough of the bar) presents a significant area where the air bubbles from previous waves are present

522 in a highly turbulent flow.

523 Despite the good agreement of penetration depth and bubbles cloud length when compared to
524 previous studies, there are other parameters and formulations in literature that our experimental data
525 do not follow so closely. Hwung et al. (1992) [37] performed a set of small-scale experiments with a
526 planar 1/15 slope measuring the air bubbles mixing in the surf zone, and provided a formula to
527 describe the vertical distribution of their concentration during the breaking process. Following this
528 formulation, the concentration of air bubbles hyperbolically decreases with water depth. Figure 9
529 shows a clear deviation of the hyperbolic function predicted by Hwung et al. (1992) [37] (Figure 9 is
530 comparable to Figure 5 in Hwung's paper) at most of the studied locations. The deviation is sharper
531 in cases where significant amounts of air bubbles were found (x from 56 to 57 m), where the voltage
532 decreases linearly or keeps constant along the first meter of water column matching the wave breaking
533 impinging jet which produces a periodic vortex at this location. The authors have observed that for
534 low air bubble concentration and low penetration depths, there is a hyperbolic distribution of air
535 bubbles along the water column, but there is also a clear deviation for larger air bubble concentration
536 and larger penetration depths. The disagreement with the hyperbolic profile predicted by Hwung et
537 al. (1992) [37] does not come just from the linear or constant distribution of the bubbles on the
538 turbulent areas, but also from the narrowly located distribution of our air bubbles. In our case, the air
539 bubble events and distribution are found between $0.08 < x_b/L_0 < 0.26$, while the data reported by Hwung
540 et al. (1992) [37] measure air bubble events between $0.34 < x_b/L_0 < 0.79$ (where x_b is the distance from
541 the breaking point position). These differences can be due to different sources, but here they have
542 been attributed to three main causes: i) the small scale of the experiments presented by Hwung et al.
543 (1992) [37] with $H=6.11$ cm and $T=1.29$ s; ii) the difference in bed slope (planar slope in Hwung et
544 al. (1992) [37] experiments vs. the barred beach profile used in the present experiments); iii) the more
545 accurate/sensitive equipment used by Hwung et al. (1992) [37] to measure the air bubbles (He-Ne
546 Laser). The three above-mentioned parameters are relevant and can significantly affect the
547 measurement of air bubble content (area and penetration depth) along the water column after
548 breaking.

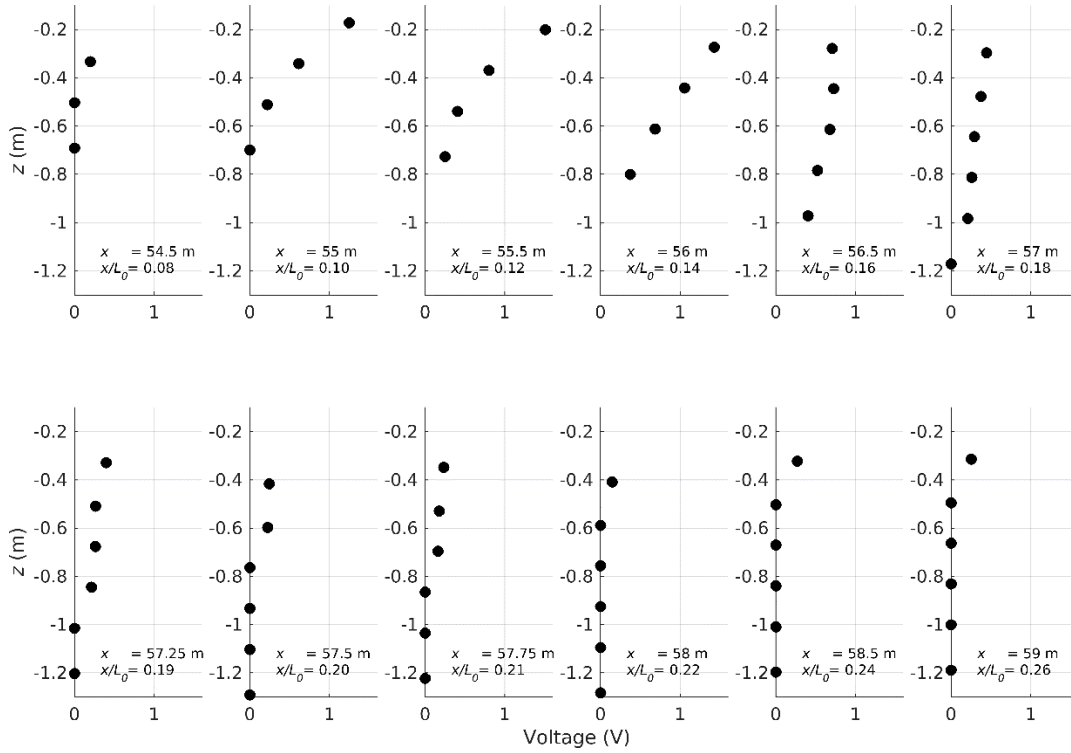


Figure 9. Time-averaged voltage over water depth for wave condition M85_4 ($H=0.85$ m and $T=4$ s).

549

550

551

5.- Discussion

552

553

554

555

The results presented here indicate that OBSs are sensitive to air bubbles. The presented data show that air bubble events collected by the OBS are phase-coherent and highly repetitive. The observations of bubble cloud length and penetration depth through OBSs are consistent with previous studies that used other instrumentation.

556

557

558

559

560

The use of a large-scale wave flume in this paper provides larger air bubble residence time and more homogeneous vertical air bubble distribution for breaking waves, in contrast to previous small-scale studies. However, the measured air bubble penetration depth and horizontal length distribution agree well with previous studies. This suggests that OBS equipment is less sensitive to air bubbles than previous equipment designed to measure void fraction and air bubble size.

561

562

563

564

565

While previous experiments have presented central air bubble distributions from the impinging point at deep water wave breaking conditions [32, 18], the data in this paper show a distribution of the air bubbles which has its centre shoreward from the impinging point. The beginning of the air bubble events from the impinging point is on average 0.4 m (from Tables 4 and 5), and most wave conditions exhibit limited air bubble events before the impinging point.

566

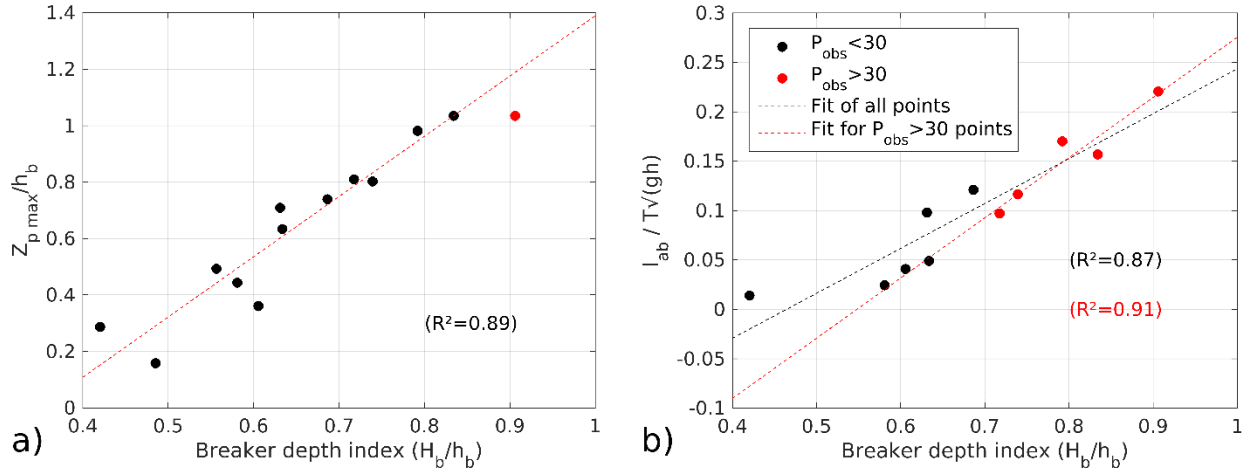
The highest value of the mean of measured peaks ($\overline{\langle Oo_p \rangle} = 0.48$ V) and the maximum ($\langle Oo_p \rangle_{\max}$)

567 = 1.49 V) of these peaks correspond to the most energetic test condition M85_4. OBS voltage
568 measurements of 0.48 V and 1.49 V correspond respectively to sediment concentrations of 5 and 16
569 g/l when calibrated for a typical medium sand with $d_{50}=0.25$ mm. Such concentration values are of
570 the same order of magnitude as suspended sediment concentrations measured close to the bed in the
571 breaking region (5 to 7 g/l are typical values of suspended sediment concentration events free of air
572 bubbles).

573 Although these extreme values correspond to the most energetic test condition M85_4,
574 nevertheless the values reported in Table 5 tell us to be very cautious when interpreting OBS data
575 collected in bubbly areas. When considering the tests for which $P_{obs}>30\%$, the mean of the computed
576 measured peaks at all stations is 0.38 V. This mean estimation can be done when considering just one
577 location for each wave condition ($\langle O_{op} \rangle_{\max}$), obtaining a mean value of 1.0 V. Both values of 0.38
578 and 1.0 V correspond, for a $d_{50}=0.25$ mm sediment, to 4.0 and 10.6 g/l respectively, which is
579 sufficiently high to induce a significant overestimation of the suspended sediment concentration and
580 flux in surf zone conditions.

581 Different parameters have been studied to forecast the air bubble distribution across the surf zone.
582 The focus is on predicting what breaking wave conditions will produce false OBS suspended
583 sediment readings, which will help to better locate the measurement equipment across the surf zone
584 in further experiments. Based on the correlations studied, the breaker depth index ($\gamma_b=H_b/h_b$) appears
585 to be the best parameter to predict the spatial air bubble distribution (represented in dimensionless
586 forms of $z_{p \max}$ and l_{ab} , computed by means of $z_{p \max}/h_b$ and $l_{ab}/T\sqrt{gh}$). Figure 10-a correlates the
587 breaker depth index with the dimensionless penetration depth, which can be used to develop a
588 predictive formula that can help users to determine the area where air bubbles will be found. The
589 collected data were fitted to a first degree polynomial equation (Equation 2) with a coefficient of
590 determination (R^2) equal to 0.89, which is plotted in Figure 10-b. The only data that were excluded to
591 produce such a polynomial equation is the data from the most energetic case (M85_4, red dot in
592 Figure 10-a), where the air bubbles were observed to reach the bottom of the profile and where
593 therefore depth-limited.

594



595 Figure 10. Correlations between breaker depth index and: a) Penetration depth, and b) the air bubble length.

596

597 Eq. 2 $Z_{p \max} / h_b = 2.135 \gamma_b - 0.745 \quad (R^2 = 0.89)$

598

599 The second applicable formulation derived from the present results is obtained from the
600 information shown in Figure 10-b. This panel presents the dimensionless air bubble cloud length
601 ($l_{ab} / T \sqrt{gh}$) for all tests as a function of the breaker depth index (with h being the absolute water
602 depth value at the toe of the wave paddle, 2.65 m). The black solid dots show the tests with small air
603 bubble distribution ($P_{\text{obs}} < 30\%$), while the red dots show the tests that have a larger distribution of air
604 bubbles ($P_{\text{obs}} > 30\%$). The black dashed line indicates the polynomial curve fit to all measured points
605 (Equation 3) with its coefficient of determination ($R^2 = 0.87$). The red dashed line presents the
606 polynomial curve fit (Equation 4) of the red dots ($R^2 = 0.91$), which from the authors' viewpoint is
607 more representative of the air bubble distribution when considering the equipment and spatial
608 resolution of the measurements.

609

610 Eq. 3 $l_{ab} / T \sqrt{gh} = 0.45 \gamma_b - 0.21 \quad (R^2 = 0.87)$

611 Eq. 4 $l_{ab} / T \sqrt{gh} = 0.61 \gamma_b - 0.33 \quad (R^2 = 0.91)$

612

613 The data here presented have been acquired using fresh water, and although there is some
614 discussion on the effects of fresh versus salt water on the size and number of air bubbles under
615 breaking wave conditions, there is a general agreement that, under salt water conditions, there is a

616 large number of bubbles with a smaller size. Cartmill and Su (1993) [38] conducted a set of laboratory
617 experiments to study the size and density of air bubbles for breaking waves using both fresh and salt
618 water. Wave groups were generated in order to produce wave breaking and bubble plumes that were
619 comparable in scale to moderate ocean waves. They reported differences in bubble size under salt and
620 fresh water conditions, with the former ones being finer. The smaller size of bubbles in salt water was
621 attributed to the coalescence of micro-bubbles in fresh water, which is inhibited by ionic repulsion of
622 salt water (fresh water air bubbles join together more easily than in salt water conditions, where the
623 ionic charges on the air bubbles' surface repel other air bubbles, thus preventing them from merging).
624 Puleo et al. (2006) [10] also noted that in salty environments where bubbles tend to be smaller, OBS
625 voltages are larger than the readings obtained using fresh water. Lastly, Anguelova and Huq (2018)
626 [39] achieved similar results, reporting an increase in the number, with smaller size, of air bubbles
627 induced by a salinity increase in the water. This effect was also attributed to the fact that air bubbles
628 tend to shatter easily and do not join again under salt water conditions. Other authors, including Wu
629 (2000) [40], claim that air bubbles in salty conditions are not smaller than in fresh water, but simply
630 that more bubbles are entrained and produced in salt water conditions. According to Wu (2000) [40],
631 the breaking process appears to be more important than bubble coalescence or shattering when
632 considering the number and size of air bubbles.

633

634 **6.- Conclusions**

635 A laboratory data set was collected in a large-scale wave flume with the objective of quantifying
636 spurious Optical Backscatter Sensor measurements produced by the presence of air bubbles. The
637 analysis has spanned different depths and locations relative to the breaking point for plunging
638 breaking waves over a fixed barred bed profile. Six OBS sensors were located on a mobile trolley
639 that was moved along the breaking area while repeating 14 selected wave conditions that produced
640 breaking waves over the barred profile. Water surface elevation was measured using Wave Gauges,
641 Acoustic Wave Gauges, Pore Pressure Transducers and velocity measurements were made using
642 Acoustic Doppler Velocimeters.

643 The OBS acquired data were processed after verifying that, in the absence of suspended sediment
644 particles, the voltage peaks of the OBS sensors were produced by air bubbles. The experimental data
645 presented confirm that the large amount of air bubbles produced at the wave breaking area have a
646 significant impact on the OBS signal. The measured OBS voltages are consistent and repeatable for
647 air bubble events across the entire measurement area. Formulations for air bubble penetration depth
648 and bubble cloud length, obtained using small-scale experiments and air bubbles measurement

649 equipment, were used to compare the acquired data. The result of this comparison was that the
650 measured characteristics of the air bubbles (penetration depth and air bubble cloud length after
651 breaking), collected under large-scale wave conditions and using OBS, lie within the range of
652 previous studies that measured air bubbles and void fraction. On the other hand, the large scale
653 experimental data set presents larger residence times of air bubbles in the water column and a more
654 homogeneous air bubble distribution after the impinging point. Considering previous information,
655 and the lower sensitivity of OBS to measure air bubbles than other equipment, the use of large scale
656 facilities is recommended in further studies.

657 The data shows that under energetic wave conditions air bubbles can produce false suspended
658 sediment concentrations even when deployed close to the bottom. The maximum mean average value
659 obtained in the time series presented is 0.48 V, while the maximum mean of the peaks measured at
660 the same location reports a value of 1.49 V. This represents 31% of the measurement range of the
661 OBS (the calibration range of this OBS was up to a maximum of 80 g/l using a sediment with $d_{50}=0.25$
662 mm, with 0.48V corresponding to values of 5 g/l, and 1.49 V to 16 g/l). Such false readings are in the
663 order of magnitude of previous suspended sand concentration measurements in surf zone conditions
664 in the absence of air bubbles (mean values of 5 to 7 g/l). The area in which the air bubbles will affect
665 OBS measurements is limited in space to the proximity of the impinging point, with a maximum
666 longitudinal distribution length of 4.5 m and a maximum vertical penetration depth of 0.98 m in the
667 present data set.

668 When large air volumes enter the water column and achieve significant penetration depths, the air
669 bubble distribution differs from the hyperbolic vertical distribution observed by Hwung et al. (1992)
670 [37]. The data presented show a linear correlation between the breaker depth index and: i) the
671 measurements by the OBSs; ii) the air bubble penetration depth; and iii) the length of the air bubble
672 cloud spreading at the surface. A linear correlation (Eq. 2 with $R^2=0.89$) was obtained to predict the
673 dimensionless penetration depth as a function of the breaker depth index, while correlations on Eq. 3
674 and 4 have been obtained to predict the dimensionless air bubble cloud length as a function of the
675 breaker depth index. These formulations will help to predict the water depth and distance from the
676 breaking location at which the air bubbles can interfere with OBS measurements for wave breaking
677 at barred beach profiles, offering a guideline for OBS usage in the surf zone.

678

680 **Acknowledgements**

681 We offer our gratitude to the CIEM staff, especially to Joaquim Sospedra for his endurance and
682 leadership. The work described in this paper was supported by the European Community's Horizon
683 2020 Programme by means of the Hydralab+ Project (contract number 654110). This paper
684 contributes to the Hydralab+ legacy together with a set of coordinated papers in other journals. Finally
685 we acknowledge the economical funding and support received by the Secretaria d'Universitats i
686 Recerca del Dpt. d'Economia i Coneixement de la Generalitat de Catalunya (Ref. 2017SGR00773).

687

688 **References**

689 [1] Masselink, G., Russell, P., Turner, I. and Blenkinsopp, C., 2009. Net sediment transport and
690 morphological change in the swash zone of a high-energy sandy beach from swash event to tidal cycle
691 time scales. *Marine Geology*, Vol. 267: 18-35.

692 [2] Alsina, J.M., van der Zanden, J., Cáceres, I. and Ribberink, J.S., 2018. The influence of wave
693 groups and wave-swash interactions on sediment transport and bed evolution in the swash zone.
694 *Coastal Engineering*, Vol. 140, 23-42.

695 [3] Downing, J.P., Sternberg, R.W. and Lister, C.R.B., 1981. New instrumentation for the
696 investigation of sediment suspension processes in the shallow marine environment. *Marine Geology*,
697 Vol. 32, 19-34.

698 [4] D & A Instrument Company, 1991. Instruction Manual, OBS-1 and 3, p. 41.

699 [5] Butt, T., Miles, J., Ganderton, P. and Russell, P., 2002. A simple method for calibrating optical
700 backscatter sensors in high concentrations of non-cohesive sediments. *Marine Geology* 192 (4), 419-
701 424.

702 [6] Downing, J.P. and Beach, R.A., 1989. Laboratory apparatus for calibrating optical suspended
703 solids sensors. *Marine Geology*, Vol. 86, 243-249.

704 [7] Downing, J.P. and Asher, W.E., 1997. The Effects of Colored Water and Bubbles on the
705 Sensitivity of OBS Sensors. American Geophysical Union, 1997 Fall Meeting, San Francisco, CA.

706 [8] Terrill, E.J, Melville, W.K. and Stramski, D., 2001. Bubble entrainment by breaking waves
707 and their influence on optical scattering in the upper ocean. *Journal of Geophysical Research*, Vol.
708 106, N° C8, 16815-16823.

- 709 [9] Smith, G.G. and Mocke, G.P., 2002. Interaction between breaking/broken waves and
710 infragravity-scale phenomena to control sediment suspension transport in the surf zone. *Marine*
711 *Geology*, Vol. 187, 329–345.
- 712 [10] Puleo, J.A., Johnson, R.V., Butt, T., Kooney, T.N. and Holland, K.T., 2006. The effect of air
713 bubbles on optical backscatter sensors. *Marine Geology*, Vol. 230: 87-97.
- 714 [11] Kalvoda, P.M., Xu, L and Wu, J., 2003. Macrobubble clouds produced by breaking wind
715 waves: A laboratory study. *Journal of Geophysical Research*, Vol. 108, C6, 3207,
716 doi:10.1029/1999JC000265
- 717 [12] Mori, N., Suzuki, T. and Kakuno, S., 2007. Experimental study of air bubbles and turbulence
718 characteristics in the surf zone. *Journal of Geophysical Research*, Vol. 112, C05014,
719 doi:10.1029/2006JC003647
- 720 [13] Bell, T.G., Landwehr, S., Miller, S.D., de Bruyn, W.J., Callaghan, A.H., Scanlon, B., Ward,
721 B., Yang, M. and Saltzman, E.S., 2017. Estimation of bubble-mediated air-sea gas exchange from
722 concurrent DMS and CO₂ transfer velocities at intermediate-high wind speeds. *Atmospheric*
723 *Chemistry and Physics*, Vol 17, Pages: 9019-9033, doi:10.5194/acp-17-9019-2017.
- 724 [14] Chanson, H., Aoki, S. and Maruyama, M., 2002. Unsteady air bubble entrainment and
725 detrainment at a plunging breaker: dominant time scales and similarity of water level variations.
726 *Coastal Engineering*, Vol. 46, 139–157.
- 727 [15] Monahan, E. and Lu, M., 1990. Acoustically relevant bubble assemblages and their
728 dependence on meteorological parameters. *IEEE Journal of Oceanic Engineering*, Vol. 15, N° 4, 340-
729 349. doi:10.1109/48.103530
- 730 [16] Deane, G. B., and Stokes, M. D., 2002. Scale dependence of bubble creation mechanisms in
731 breaking waves. *Nature* 418, 839–844, doi:10.1038/nature00967
- 732 [17] Lamarre, E., 1993. An experimental study of air entrainment by breaking waves. PhD thesis,
733 Department of Civil and Oceanographic Engineering. Cambridge, MA: MIT Press. doi:
734 10.1575/1912/5509
- 735 [18] Lamarre, E., Melville, W.K., 1992. Instrumentation for the measurement of void-fraction in
736 breaking waves: Laboratory and field results. *IEEE Journal of Oceanic Engineering*, Vol. 17, N° 2,
737 204–215. doi: 10.1109/48.126977
- 738 [19] Hall, K. R., 1990. Aeration in rubble-mound breakwater models. *J. of Water, port, Coastal*
739 *and Ocean Eng., ASCE*, Vol. 116, pp. 400-405.

- 740 [20] Ting, F. C. K., and Kirby, J. T., 1995. Dynamics of surf zone turbulence in a strong plunging
741 breaker, *Coastal Engineering*, Vol. 24, 177–204.
- 742 [21] Kiger, K.T. and Duncan, J.H., 2012. Air-Entrainment Mechanisms in Plunging Jets and
743 Breaking Waves. *Annual Review of Fluid Mechanics*, Vol. 44, 563–596.
- 744 [22] van der A, D.A., van der Zanden, J., O’Donoghue, T., Hurther, D., Cáceres, I., McLelland, S.
745 and Ribberink, J.S., 2017. Large-scale laboratory study of breaking waves hydrodynamics over a
746 fixed bar. *Journal of Geophysical Research: Oceans*. Vol. 122(4), 3287-3310,
747 doi:10.1002/2016JC012072
- 748 [23] van der Zanden, J., van der A, D. A., Cáceres, I., Hurther, D., McLelland, S.J., Ribberink, J.
749 and O’Donoghue, T., 2018. Near-bed turbulent kinetic energy budget under a large-scale plunging
750 breaking wave over a fixed bar. *Journal of Geophysical Research: Oceans*. Vol. 123,
751 doi:10.1002/2017JC013411
- 752 [24] Battjes, J.A., 1974. Surf similarity. *Proceedings of 14th Coastal Engineering Conference*, Co-
753 penhagen, Denmark, 466–480.
- 754 [25] Smith, E. R., and Kraus, N. C., 1991. Laboratory study of wave-breaking over bars and
755 artificial reefs. *Journal of Waterway, Port, Coastal, and Ocean Engineering*, 117(4), 307–325.
756 doi:10.1061/(asce)0733-950x(1991)117:4(307)
- 757 [26] Mori, N., Suzuki, T. and Kakuno, S., 2007. Noise of acoustic doppler velocimeter data in
758 bubbly flow, *J. Eng. Mech.*, 133(1), 122–125.
- 759 [27] Tucker, M.J. and Pitt, E.G., 2001. *Waves in Ocean Engineering*. Elsevier Ocean Engineering
760 Book Series, Vol. 5, Amsterdam, 521 pp.
- 761 [28] Neumeier, U, 2006. Processing of wave data from pressure sensors.
762 <http://neumeier.perso.ch/matlab/waves.html>.
- 763 [29] Goring, D.G. and Nikora, V.I., 2002. Despiking acoustic doppler velocimeter data. *Journal*
764 *of Hydraulic Engineering*, 128(1): 117-126.
- 765 [30] Longuet-Higgins, M., 1953. Mass transport in water waves. *Philosophical Transactions of*
766 *the Royal Society A* 245, 535-581. doi: 10.1098/rsta.1953.0006.
- 767 [31] Van den Bremer, T.S. and Breivik, O., 2017. Stokes drift. *Philosophical Transactions of the*
768 *Royal Society A*, 376, 20170104. doi:10.1098/rsta.2017.0104
- 769 [32] Blenkinsopp, C.E. and Chaplin, J.R., 2007. Void fraction measurements in breaking waves.
770 *Proceedings of the Royal Society A.*, Vol. 463, 3151-3170, doi:10.1098/rspa.2007.1901.

- 771 [33] Lim, H., Chang, K, Huang, Z. and Na, B., 2015. Experimental study on plunging breaking
772 waves in deep water. *Journal of Geophysical Research*, Vol. 120, 2007-2049,
773 doi:10.1002/2014JC010269.
- 774 [34] Alsina, J.M., Padilla, E.M. and Cáceres, I., 2016. Sediment transport and beach profile
775 evolution induced by bi-chromatic wave groups with different group periods. *Coastal Engineering*,
776 Vol. 114, 325-340.
- 777 [35] Cáceres, I. and Alsina, J.M., 2012. A detailed, event-by-event analysis of suspended sediment
778 concentration in the swash zone. *Continental Shelf Research*, Vol. 41, pp. 61-76.
- 779 [36] Chanson, H. and Lee, J.F., 1997. Plunging jet characteristics of plunging breakers. *Coastal*
780 *Engineering*, Vol. 31, 125–141.
- 781 [37] Hwung, H. H., Chyan, J.M. and Chung, Y.C., 1992. Energy dissipation and air bubbles
782 mixing insider the surf zone. *International Conference on Coastal Engineering*, 1992.
- 783 [38] Cartmill, J.W. and Su, M.Y., 1993. Bubbles size distribution under saltwater and freshwater
784 breaking waves. *Dynamic of Atmospheres and Oceans*, Vol. 20, 25-31. doi:10.1016/0377-
785 0265(93)90046-A.
- 786 [39] Anguelova, M.D. and Huq, P., 2018. Effects of salinity and bubble cloud characteristics.
787 *Journal of Marin Science and Engineering*, Vol. 6, 1-17, doi:10.3390/jmse6010001
- 788 [40] Wu, J., 2000. Bubbles produced by breaking waves in fresh and salt waters. *Journal of*
789 *Physical Oceanography*, Vol. 30, 1809-1813.